Journal of Non-Crystalline Solids 641 (2024) 123096

Contents lists available at ScienceDirect

Journal of Non-Crystalline Solids

journal homepage: www.elsevier.com/locate/jnoncrysol

# Quantitative structural characterization of $LiNbO_3$-$SiO_2$ glass-ceramics by multinuclear solid-state NMR

Henrik Bradtmüller [a,*], Qiuju Zheng [b], Hellmut Eckert [c], Edgar D. Zanotto [a]

[a] Department of Materials Engineering, Vitreous Materials Laboratory, Federal University of São Carlos, CP 676, 13565-905 São Carlos, SP, Brazil
[b] Key Laboratory of Processing and Testing Technology of Glass & Functional Ceramics of Shandong Province, School of Materials Science and Engineering, Qilu University of Technology (Shandong Academy of Sciences), Jinan 250353, China
[c] São Carlos Institute of Physics, University of São Paulo, Avenida Trabalhador Sãocarlense 400, São Carlos 13566-590, SP, Brazil

ARTICLE INFO

*Keywords:*
NMR
Glasses
Crystallization
$^{93}Nb$
$LiNbO_3$
Glass ceramics
Nanocomposites

ABSTRACT

This study presents a detailed structural analysis of the glass-to-crystal transition in the technologically important $LiNbO_3$–$SiO_2$ glass system, focusing on the composition $35Li_2O$–$25Nb_2O_5$–$40SiO_2$ known for its exceptional second harmonic generation (SHG) response in glass-ceramics. We develop a comprehensive solid-state NMR protocol to quantify major and minor fractions of elusive nanocrystalline phases and the residual glass composition, overcoming limitations of techniques such as X-ray diffraction and Raman spectroscopy. By employing $^7$Li satellite transition difference spectroscopy and $^{93}$Nb magic-angle spinning (MAS) NMR, we achieve quantification of crystalline fractions down to 1%. By combining all the complementary $^6$Li, $^7$Li, $^{29}$Si, and $^{93}$Nb MAS NMR experiments, we also deduce the composition of the residual glass. Short crystallization times (up to 120 min) at 640 °C result in nanocrystalline $LiNbO_3$, whereas crystallization for 1440 min at this temperature additionally yields two $Li_2Si_2O_5$ polymorphs and $Li_2SiO_3$. $^7$Li spin echo and $^7$Li{$^{93}$Nb} W-RESPDOR NMR spectroscopy indicate that $LiNbO_3$ crystallizes in specific domains leaving behind $SiO_2$-rich residual glassy domains. This work offers a time-efficient and versatile NMR protocol for characterizing crystalline and residual glass components in nanocrystalline glass-ceramics in the $LiNbO_3$–$SiO_2$ system and beyond, providing valuable insights into the crystallization process which is not possible with other techniques.

## 1. Introduction

Lithium niobate is a ferroelectric material featuring a unique combination of nonlinear optical, electro-optic, and piezoelectric properties. This makes it a versatile material with applications ranging from telecommunications and signal processing to medical imaging and quantum computing. Its role in various optical devices contributes significantly to the advancement of technology in these fields [1]. Especially interesting in this regard is the production of nanocomposites where the properties of a second-harmonic generating material like $LiNbO_3$ can be combined with those of a host matrix, broadening these materials' application appeal.

Commonly, $LiNbO_3$ nanocomposites are produced through wet chemical techniques, such as the sol-gel process, where the stabilization of $Nb^{5+}$ in the aqueous or ethanolic solution is the key step resulting in thin films [2]. An exciting alternative route is the production of $LiNbO_3$-containing glass-ceramics through controlled crystallization of glass, resulting in a fine-grained structure incorporating the nanocrystalline phases within the residual vitreous matrix [3]. An advantage of this route is that the three-dimensional shape of the resulting material can be easily controlled in the vitreous state and the associated high speed of the glass processing techniques allow the production of thousands of pieces in a short time. Further, glass-ceramics may offer synergistic effects compared to either glassy or crystalline compounds which may increase the nonlinear response of the resulting material even further [4,5]. Currently, suitable glass-ceramic systems exhibiting such synergistic effects are widely investigated candidates for optimized nonlinear optical properties such as second harmonic generation. Their crystallization can be controlled by subjecting the glass to nucleation and growth heat treatments which impart unique and advantageous nanostructures and properties to glass-ceramics. Their corresponding niobiosilicate precursor glasses are also interesting materials

---

* Corresponding author at: Department of Materials Engineering, Federal University of São Carlos, Rod. Washington Luis, km 235 C.P. 676, 13.565-905 São Carlos, SP, Brazil.

*E-mail address:* mail@bradtmueller.net (H. Bradtmüller).

https://doi.org/10.1016/j.jnoncrysol.2024.123096
Received 24 March 2024; Received in revised form 19 June 2024; Accepted 20 June 2024

themselves, with applications in the field of microwave technology, where the composition and structure on the atomic level directly control the dielectric properties [6,7].

The structural characterization of glass-ceramic nanocomposites is notoriously difficult since the application of commonly used X-ray diffraction methods is severely limited for both, the glassy and the nanocrystalline components. To the present date, few detailed studies of quantitative phase content have been done on nanostructured glass-ceramics, based on Rietveld analysis of the crystalline inventory, from which the composition of the residual glassy phase could be deduced, e.g., in lithium disilicate dental glass-ceramics [8,9]. While this approach turned out to be very successful in that case, the Rietveld analysis encounters limitations when the crystalline phases are nano-sized, the crystallized volume fractions are small, or multiple phases are formed. Also, in such studies, information about the residual glass composition is extracted mostly in an indirect way. In principle, more direct information about the glassy phase itself can be obtained using solid-state nuclear magnetic resonance (NMR), which is a powerful tool capable of providing structural details on the atomic level. While NMR has been applied to glass-ceramic characterization in various technologically important non-stoichiometric glass-ceramic systems, [10-18] to the present date, its application to $Nb_2O_5$-containing glasses and glass-ceramics has been limited owing to the properties of the NMR active $^{93}$Nb isotope in disordered environments [19-27]. Specifically, the resolution of these spectra is compromised by the simultaneous presence of strong quadrupole and chemical shift anisotropy interactions, rendering the spectroscopic analysis and differentiation of Nb local environments very challenging.

In the present contribution, we monitor the glass-to-crystal transition in the $Li_2O$–$Nb_2O_5$–$SiO_2$ system. We focus on the non-stoichiometric composition $35Li_2O$–$25Nb_2O_5$–$40SiO_2$, which was previously shown to crystallize spherulitic $LiNbO_3$ crystals upon annealing, resulting in an isotropic bulk second harmonic generation response [28]. This system is characterized by the crystallization of lithium niobate, leaving behind a residual glassy material whose composition and structural features have not been examined so far. Here we develop a comprehensive, straightforward, and time-effective solid-state NMR strategy to quantify the degree of crystallinity in $LiNbO_3$–$SiO_2$-based glass-ceramic nanocomposites, as well as the elemental content and the structural features of the residual glass left behind at different annealing stages. We propose that this strategy will be generally applicable to mechanistic crystallization studies of lithium-containing glass-ceramic systems.

## 2. Materials and methods

### 2.1. Sample preparation and characterization

A 30 g batch of glass with composition $35Li_2O$–$25Nb_2O_5$–$40SiO_2$ was prepared as reported previously [26] and its composition analyzed by inductively coupled plasma optical emission spectrometry (ICP-OES) yielding $Li_2O$, $Nb_2O_5$, and $SiO_2$ contents of 34.7, 25.5, and 39.8 mol%, respectively, which agree with the desired nominal composition within 0.5 mol%. To produce fine-grained glass-ceramics, the ideal nucleation temperature, $T_n$, was determined through a series of heat treatments from $T_g$ (556 °C) to $T_g$ + 40 °C, see Figure S1. We found that heat treatment at 575 °C results in the lowest DSC crystallization peak temperature and the largest first crystallization peak area at 640 °C. Glass-ceramic samples were thus prepared by two-stage nucleation-crystallization heating of bulk samples at 575 °C for 3 h and variable treatment times at 640 °C. Using this protocol, we identified two time thresholds, one at 45 min, which marks the onset of surface crystallization and results in opalescent specimens, and another at 70 min, beyond which bulk crystallization takes over and non-transparent specimens are produced. Following the desired annealing times (45, 70, 120 (2 h), and 1440 min (24 h)), samples were quenched by fast removal from the furnace. Given that surface crystallization leads to a net preferred orientation of the ferroelectric crystallites at the surface which is quite different in the bulk, the surface layer of the glass-ceramics was removed by polishing before further characterization.

Differential scanning calorimetry data were obtained using a Netzsch DSC 404 calorimeter equipped with a TASC 414/3 controller operated under nitrogen atmosphere at a heating rate of 10 K/min. Freshly powdered samples of about 30 mg in aluminum or platinum crucibles were employed, using powdered $Al_2O_3$ as a reference material. X-ray diffraction experiments were carried out on powdered samples on a Bruker D8 ADVANCE Da Vinci/3kw diffractometer with Cu target ($K_\alpha$ wavelength) at working voltage and current of $\leq$ 40 kV and $\leq$ 40 mA, respectively. Diffraction data was collected with a 0.067-degree step size and 1 s integration time. Raman spectra were measured in the 100 – 1400 $cm^{-1}$ range with an acquisition integration time of 100 s and 2 cycles using a LabRAM HR 800 Raman spectrophotometer (Horiba Jobin Yvon) equipped with a CCD detector (model DU420A-OE-325) and a He–Ne laser (632.81 nm). Scanning electron microscopy (SEM, Gemini 500, Zeiss, Germany) was used to characterize the cross-sectional morphology of the samples. Results are shown in the Supporting Materials Section.

### 2.2. Solid-State NMR

$^{29}$Si MAS NMR spectroscopy was performed at 5.64 T on an Agilent DD2 spectrometer (48.15 MHz Larmor frequency). The experiments were carried out in a commercial 7.5 mm probe at a MAS frequency of 5.0 kHz. Each spectrum was recorded with 128–136 scans using an excitation pulse length of 7 μs and an optimized recycle delay of 600 s, which was found to provide quantitative spectra as tested by variable relaxation delay experiments. The chemical shift is reported with respect to TMS (0 ppm). $^{93}$Nb MAS NMR experiments were conducted at 14.10 T (146.80 MHz Larmor frequency) in a 1.3 mm double-resonance probe at a MAS rate of 60.0 kHz and a nutation frequency of $\upsilon_{rf}$ = 150 kHz measured on a liquid sample of $NbCl_5$ in acetonitrile. For the rotor-synchronous Hahn-echo spectra, excitation pulse lengths of 0.6 μs and 1.2 μs were used and a recycle delay of 0.1 s proved sufficiently long to produce quantitative spectra (no spectral changes were observed beyond 0.05 s). To minimize coil ringing effects, spectra were acquired after 2 rotor cycles. Spectra were fitted according to the Czjzek model (Eq. (1a)) and the extended Czjzek model (Eq. (1b)) implemented in the ssNake simulation program v1.5b [29].

As indicated by the pulse lengths utilized, the $^{93}$Nb nuclei in the glasses are within a regime between selective and non-selective excitation. Systematic pulse parameter variations and SIMPSON simulations were done to test the effect of rotor-synchronized Hahn spin echo pulse parameters on the $^{93}$Nb NMR lineshapes and quantitative ratios of Nb populations in the glassy and crystalline phases. Based on these results the chosen pulse lengths were sufficiently short to not affect the lineshape parameters. Chemical shifts were referenced against a saturated solution of $NbCl_5$ in acetonitrile (MeCN), using solid $LiNbO_3$ ($\delta_{iso}^{CS}$ = −1004 ppm) as a secondary standard.

The $^{93}$Nb MAS-NMR spectra were modeled according to the Czjzek model, which assumes a random distribution of electric field gradient (EFG) tensors around about a central value of zero and can be approximated by a probability density function expressed in terms of $C_Q$ and $\eta_Q$:

$$f(C_Q, \eta_Q) = \frac{C_Q^{d-1}\eta_Q}{\sqrt{2\pi}\sigma^d}\left(1 - \frac{\eta_Q^2}{9}\right)\exp\left\{-\frac{C_Q^2}{2\sigma^2}\left(1 + \frac{\eta_Q^2}{3}\right)\right\} \tag{1a}$$

Here, $\eta_Q$ is the asymmetry parameter of the EFG tensor, $d$ is the number of independent tensor components (typically 5, as in the present work), and $\sigma$ is the standard deviation of the multidimensional Gaussian distribution. This model was later extended for cases in which the center of the distribution does not correspond to 0 for $C_Q$ and $\eta_Q$ for small $\sigma$, but rather finite values denoted $C_{Q,0}$ and $\eta_{Q,0}$:

$$f(C_Q,\eta_Q)=\frac{C_Q^{d-1}\eta_Q}{\sigma^d}\left(1-\frac{\eta_Q^2}{9}\right)\int\int\int \mathrm{d}\alpha\,\sin(\beta)\mathrm{d}\beta\mathrm{d}\gamma\times\exp\left\{-\frac{1}{2\sigma^2}\left[C_{Q,0}^2\left(1+\frac{\eta_Q^2}{3}\right)+C_Q^2\left(1+\frac{\eta_Q^2}{3}\right)-\frac{2}{\sqrt{3}}C_QC_{Q,0}\left(\sqrt{3}a_{11}+\eta_{Q,0}a_{15}+\eta_Q\left(a_{51}+\frac{\eta_{Q,0}a_{55}}{\sqrt{3}}\right)\right)\right]\right\} \tag{1b}$$

Here, $\alpha$, $\beta$, and $\gamma$ are the Euler angles of the EFG tensor of a given crystallite in the rotor axis system and $a_{ij}$ describe the angular dependence of EFG tensor components which can be found in the literature [30]. $^6$Li MAS NMR experiments were carried out at 14.1 T using a commercial 3.2 mm double-resonance probe at a MAS rate of 10.0 kHz. Using an excitation pulse length of 8.33 µs a total of 16 – 1536 scans were collected. $^6$Li chemical shifts are referenced against a 1 M LiCl solution (0 ppm). $^7$Li satellite transition spectroscopy (SATRAS)[31] was performed at 14.10 T (233.18 MHz) at $\upsilon_{MAS} = 10.0$ kHz for the analysis of the spinning sideband patterns arising from the non-central (satellite) $^7$Li Zeeman transitions. SATRAS difference spectra were produced as previously described [13] through subtraction of a SATRAS spectrum composed of the fast relaxing vitreous part (obtained by a SATRAS measurement of the sample using a short recycle delay $d_1 = 0.1$ s) from the SATRAS spectrum of the fully relaxed sample ($d_1 = 160$ s), leaving just the spectral components not present in the reference spectrum. Prior to the subtraction both spectra were normalized such that the outermost spinning sidebands – arising exclusively from the $^7$Li spins in vitreous environments – match in intensity. For obtaining reliable results it is necessary to record both of these SATRAS NMR spectra as two consecutive experiments under identical conditions, as every change in MAS spinning rate, transmitter offset frequency, nutation frequency, etc. may result in artifacts. $^7$Li chemical shifts are reported with respect to a 1 M LiCl solution (0 ppm).

Static $^7$Li spin-echo decay (SED) NMR experiments were conducted on the Agilent spectrometer in a 4 mm triple-resonance probe. Measurements were performed at −100 °C to remove contributions from dynamic relaxation to the echo decay using the Hahn spin-echo sequence ($t_{\pi/2} - \tau_1 - t_\pi - \tau_1$) as described in detail elsewhere [32]. In order to reduce radio frequency amplitude gradients, only the center third of the used 4.0 mm rotors was filled with sample. A nutation frequency of 6.25 kHz, as measured on a 0.1 M solution of LiCl, proved sufficiently low to provide the required selective central transition (CT) excitation in agreement with prior numerical SIMPSON simulations, while being sufficiently high to completely invert the spins contributing to the rather wide static CT spectra. Decay curves of normalized intensity $\frac{I(2\tau_1)}{I(0)}$ versus dipolar mixing time, $2\tau_1$, were modeled as Gaussians, according to

$$\ln\left(\frac{I(2\tau_1)}{I(0)}\right) = -\frac{M_{2E(\text{Li-Li})}}{2}(2\tau_1)^2. \tag{2}$$

as proven previously to be valid at sufficiently short dipolar mixing times, both for multi-spin systems of spin-½ nuclei [33] and for multi-spin systems of quadrupolar nuclei with selective excitation of the central $m = ½ \leftrightarrow m = -½$ coherence [32,34].

Here the second-moment $M_{2E(\text{Li-Li})}$ can be calculated [34] via the van-Vleck equation [35]

$$M_{2E(\text{Li-Li})} = f\left(\frac{\mu_0}{4\pi}\right)^2\gamma_{^7\text{Li}}^4\hbar^2\sum_{i\neq j}\frac{1}{r_{ij}^6}, \tag{3}$$

where the numerical prefactor $f$ is 0.9562 for $^7$Li with $I = 3/2$ for selective excitation of the central Zeeman transition [36]. In addition, the $M_2$ value must be scaled by the natural abundance factor of 0.9258 of the $^7$Li isotope.

$^7$Li{$^{93}$Nb} dipolar recoupling experiments were performed with the Rotational-Echo Saturation-Pulse Double-Resonance (RESPDOR) sequence [37], which was recently modified by us employing wideband uniform rate with smooth truncation (WURST) pulses [38] for saturation (W-RESPDOR) [39] at 14.10 T and $\upsilon_{MAS} = 20.0$ kHz in a 2.5 mm triple-resonance probe. $^7$Li excitation and refocusing pulse lengths optimized on the sample were 4.0 and 8.0 µs. A suitable WURST saturation pulse for the $^{93}$Nb spin-system was found through numerical simulations (using the SIMPSON package [40]) with 8 rotor-cycles duration (400 µs), a shape parameter of $N = 80$, and a sweep width of 450 kHz at the highest possible experimental nutation frequency of 53.0 kHz (< 10% power reflection). The experimental W-RESPDOR curves were analyzed through fits to the data in the initial dipolar evolution regime ($\Delta S/S_0 \leq 0.2$) using a recently derived parabolic approximation of the initial dephasing regime [26]

$$\frac{\Delta S}{S_0}(\text{random}) \approx \frac{2}{3\pi^2}M_{2(\text{Li-Nb})}(n\tau_r)^2, \tag{4}$$

where $n\tau_r$ is the dipolar mixing time defined by the product of the number of rotor cycles with the rotor period. Eq. (4) implies, as an approximation, a dephasing independent of the geometry of a multi-spin system at sufficiently short dipolar mixing times. Here, $M_{2(\text{Li-Nb})}$ is the heteronuclear dipolar second moment. This value can be compared with the theoretical van Vleck value, calculated for the heteronuclear case via:

$$M_{2(\text{Li-Nb})} = \frac{33}{5}\left(\frac{\mu_0}{4\pi}\right)^2\gamma_{\text{Nb}}^2\gamma_{\text{Li}}^2\hbar^2\frac{1}{N_{\text{Li}}}\sum_{i=1}^{N_{\text{Li}}}\sum_{j=1}^{N_{\text{Nb}}}\frac{1}{r_{\text{Li-Nb}}^6} \tag{5}$$

In this expression, $\gamma_{\text{Li}}$ and $\gamma_{\text{Nb}}$ are the gyromagnetic ratios of the observed nucleus $^7$Li and the recoupled spin-9/2 nucleus $^{93}$Nb, respectively.

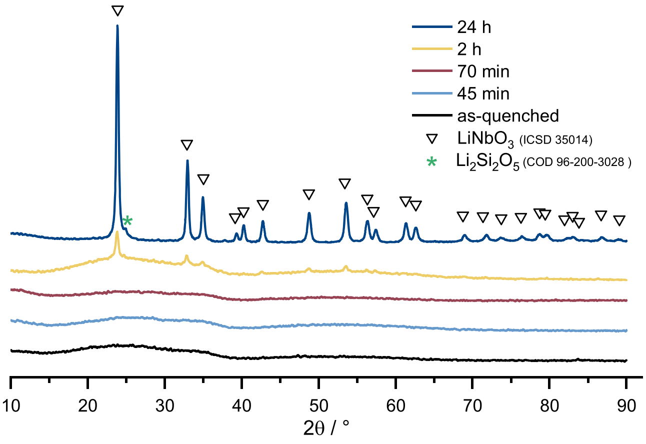

**Fig. 1.** Powder X-ray diffractograms of the specimens under study. Triangles indicate the peak positions of crystalline LiNbO$_3$ according to the ICSD entry n° 35,014. The asterisk indicates one of the principal peak positions of crystalline Li$_2$Si$_2$O$_5$, according to the Crystallography Open Database (COD) entry n° 96-200-3028.

## 3. Results and discussion

### 3.1. Glass characterization

Fig. 1 shows the X-ray diffraction patterns of the samples under study.

The diffractogram of the as-quenched glass presents broad halos over the 15 – 65° region and the absence of narrow bands, suggesting the specimen is fully vitreous. The same is observed up to a heat treatment time of 70 min. Upon longer annealing times, narrow bands appear in the diffraction pattern, with a main band at 23.85°, matching the ICSD entry 35,014 for $LiNbO_3$ [41]. Additionally, a small shoulder can be observed at 24.91° in the diffractogram after 24 h annealing time which is likely one of the three characteristic main bands of $Li_2Si_2O_5$, whereas the ones at 23.73° and 24.26° are masked by the main $LiNbO_3$ diffraction peak at 23.85°

Fig. 1 illustrates the expected diffraction peak linebroadening due to the nanocrystalline character of the $LiNbO_3$ component. Based on the linewidth of the (012) reflection at 23.85°, we obtain scattering domains of 27 and 28 nm for samples with annealing times 2 h and 24 h, respectively, using the Scherrer equation $\varnothing = \frac{K\lambda}{\beta\cos\theta}$ – where $\varnothing$ is the mean length of the ordered domains, $K = 0.9$ is an assumed shape factor, $\lambda = 154.06$ pm, the wavelength of the Cu $K_\alpha$ X-rays, and $\theta/2$ is the Bragg angle, see Table 1. These values stand in excellent agreement with the size of the crystallites seen in the SEM images of the glass-ceramics (see, Figure S2) and a previous study that reported the formation of $LiNbO_3$ spherulites of about 30 nm in diameter in the same glass system [42].

### 3.2. Differential scanning calorimetry

Figure S3 (see supporting materials) shows the DSC traces of the glass-ceramics demonstrating the invariance of $T_g$ of the residual glass at annealing times between zero and 2 h (Table 1). For the sample crystallized for 24 h, no glass transition event could be observed up to a temperature of 600 °C. In another DSC experiment up to higher temperatures, the onset of a very subtle endothermic event could be observed around 630 °C which varied around ±20 °C for individual runs. However, due to significant baseline artifacts, we refrain from assigning it to a glass transition. Further, a crystallization peak can be observed centered at 883 °C and subsequently a melting peak near 955 °C. An XRD experiment of the sample after the DSC measurement shows the formation of $SiO_2$ (cristobalite) next to $LiNbO_3$, see Figure S4.

### 3.3. Raman scattering

Fig. 2 shows the Raman spectra of the samples under study. The spectrum of the as-quenched glass shows vibrational modes near 250, 650, 850, and 1050 $cm^{-1}$ and was discussed in our previous contribution [26]. The low-frequency region ($< 350$ $cm^{-1}$) is related to Nb-O collective modes while the bands near 650 and 850 $cm^{-1}$ correspond to stretching modes of the $[NbO_x]$ species [43]. The high polarizability of the Nb-O vibrations mostly masks the vibrational modes of the silicate units, which would normally be observed over the frequency regions of 470 – 665 and 950 – 1120 $cm^{-1}$. For the sample subjected to crystallization heat treatment for 45 min at 640 °C the spectrum is identical to that of the glassy precursor, suggesting the absence of nanocrystalline lithium niobate. The thermal treatment of the glass for longer times produces significant changes in the Raman spectra, most notably the appearance of sharp peaks near 160, 200, 300, 425, and 620 $cm^{-1}$ which agree with the spectral features of $LiNbO_3$[44, 45], and increase in intensity with increasing annealing time.

The absence of any variation of these spectra in the 900–1120 $cm^{-1}$ range for the samples annealed between zero and 2 h indicates that the scattering intensity in this spectral region is dominated by the Si-O vibrations involving the non-bridging O atoms of the $Si^2$ and $Si^3$ units (in the terminology used here the superscript denotes the number of bridging oxygen atoms linked to the silicate tetrahedra). This conclusion is also consistent with the reduction of this intensity in the sample treated for 24 h, where a large fraction of the material has crystallized (see below). Consequently, the spectrum reveals the partial disappearance of Si-O stretching vibrations involving the non-bridging O atoms of the $Si^2$ and $Si^3$ units in the glass. The spectrum observed for this particular sample contains all of the bands previously published (and assigned based on comparative single-crystal work [44,45]) for nanocrystalline lithium niobate. Specifically, we note that the bands near 620 $cm^{-1}$ ($A_1(Z)$ non-degenerate TO mode), 420 $cm^{-1}$ (E(X, Y) degenerate TO or LO mode), and 380 $cm^{-1}$ (another E(X, Y) degenerate TO or LO mode) as well as the sharp Raman peaks observed in the lower wave number range clearly evidence the appearance of lithium niobate in all samples heated for longer periods than 45 min. Also, in the specimen annealed for 24 h, a weak peak observed at 1106 $cm^{-1}$ evidences the formation of crystalline lithium disilicate.

Based on Fig. 2, we can conclude that Raman spectroscopy is significantly more sensitive for the detection of nanocrystalline lithium niobate than X-ray diffraction. However, the Raman spectra are uninformative concerning the structure of the residual glass left behind after ceramization for 24 h. As discussed below, this issue is most effectively addressed by solid-state NMR.

### 3.2. $^{29}Si$ MAS NMR

Fig. 3 shows $^{29}Si$ MAS NMR spectra of the $35Li_2O–25Nb_2O_5–40SiO_2$ glass and the glass-ceramics and Table 2 shows a summary of the NMR parameters from the deconvolutions.

The signal of the glass is centered around −83 ppm and was deconvoluted into three Gaussian components corresponding to $Si^2$, $Si^3$, and $Si^4_{1Nb}$ groups, using the same physical constraints as those used in our recent contribution [26].

Here, the subscript denotes the number of heteroatoms in the second coordination sphere. For the original glass, this analysis resulted in 28% $Si^2$, 62% $Si^{3,}$ and 10% $Si^4$ units linked to Nb resulting in an average degree of polymerization $<n> = 2.82$. This value is significantly higher than that expected from the $Li_2O/SiO_2$ ratio, indicating a partial association of lithium with the niobium oxide component as a charge compensator. As previously discussed, this observation is consistent with a network former character of niobium oxide [26]

The spectra of the glass-ceramics heat treated for 45 and 70 min are essentially identical to the one of the base glass, whereas after 2 h of crystallization treatment, the formation of a shoulder near −109 ppm can be observed. For this spectrum, the deconvolution model was amended by a fourth Gaussian component corresponding to $Si^4$ groups predominantly linked to Si (e.g. $Q^4$). Finally, the spectrum of the 24 h sample clearly shows no more contribution due to $Si^2$ units, but instead the contribution of the $Si^4$ component is strongly enhanced, producing a significant increase in the average degree of polymerization in the residual glassy material ($<n> = 3.68$). The chemical shift of this new $Si^4$ unit (−109 ppm) is consistent with mostly $Si^4$-O-$Si^4$ and the absence of $Si^4$-O-$Si^3$ or $Si^4$-O-Nb connectivity of this species. We conclude that this unit is part of a glassy $SiO_2$-like microphase left behind by the crystallization of lithium niobate via extraction of the lithium content from the original glass.

**Table 1**
Glass transition temperatures for the as-quenched glass and the residual glass in the glass-ceramics and scattering domain size.

| Sample | $T_g$ / °C (± 5 °C) | $\varnothing$ / nm (±5) |
|---|---|---|
| 0 min | 557 | – |
| 45 min | 559 | – |
| 70 min | 560 | – |
| 2 h | 559 | 27 |
| 24 h | – | 28 |

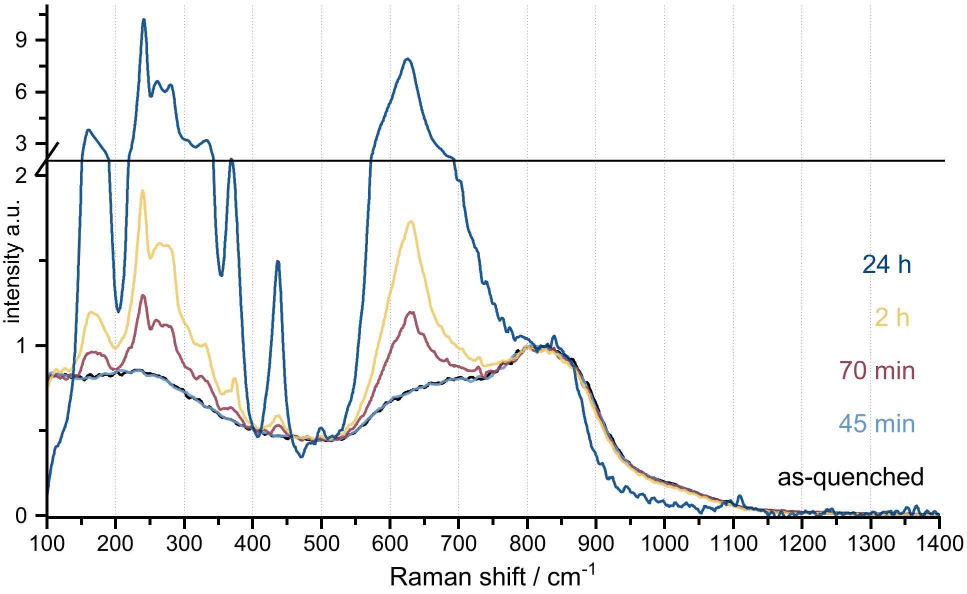

**Fig. 2.** Raman spectra of $35Li_2O–25Nb_2O_5–40SiO_2$ glass and glass-ceramics after heat treatment for the times indicated in the figure.

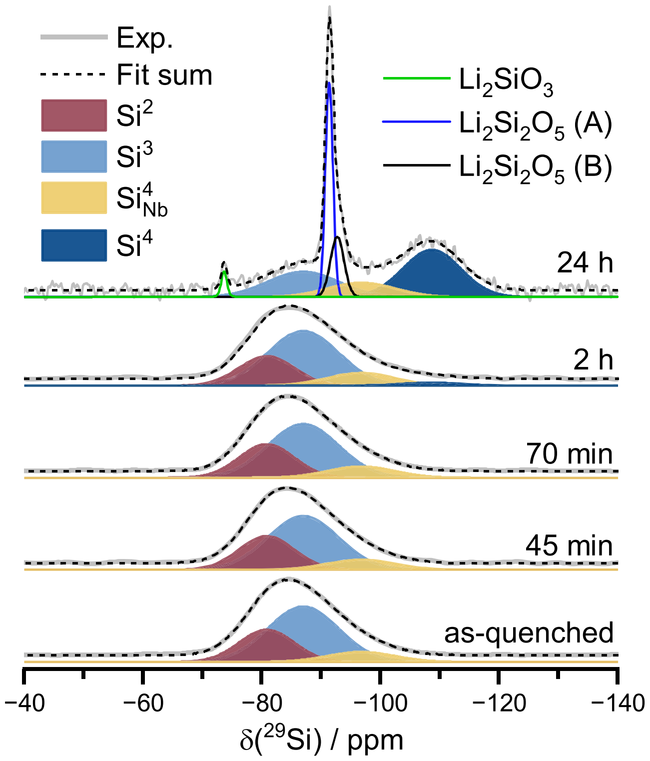

**Fig. 3.** $^{29}$Si MAS NMR spectra of $35Li_2O–25Nb_2O_5–40SiO_2$ glass and glass-ceramics under study.

Typically, the spin-lattice relaxation times of $^{29}$Si nuclei in crystalline substances, such as the lithium silicates studied here, are much longer than the employed recycle delay of 600 s. The presence of paramagnetic impurities such as $Cu^{2+}$, $Fe^{3+}$, $Mn^{2+}$ or $Nb^{4+}$, is known to significantly reduce relaxation times in glassy and crystallized materials when present at concentrations above 500 ppm. In our samples, ICP-OES analysis indicated Cu and Fe concentrations of approximately 75±5 and 42±5 ppm, respectively, while Mn levels were below the detection limit of 5 ppm. Given these low concentrations, we infer that the relatively short $^{29}$Si spin-lattice relaxation times observed are likely due to the presence of trace amounts of $Nb^{4+}$ (>500 ppm).

Further, all samples show a discrete component near −97 ppm, which is attributed to $Si^4_{Nb}$ species. Also, there are three narrow components near −73.3, −91.4, and −92.8 ppm. These features were modeled by Gaussian lineshapes and correspond to $Li_2SiO_3$, and two different polymorphs of $Li_2Si_2O_5$, respectively. It should be further noted, that contrary to the XRD data, the amount of crystalline lithium silicates detected by $^{29}$Si MAS NMR is, in fact, significant, which may indicate that their detection by XRD is impeded by nanocrystallinity. We also note that the detection sensitivity of NMR for these phases is superior to that of Raman spectroscopy. This may arise from the fact that the Raman spectra are completely dominated by the $NbO_x$ vibrations, which display much stronger variations in bond polarizability as compared to the Si-O valence modes of the silicate tetrahedra.

The results clearly indicate that the crystallization of lithium niobate results in a net re-polymerization of the residual glassy material. However, the residual glassy phase is not homogeneous but contains $Si^4$ ($Q^4$) domains with a $T_g$ value not revealed within the measurement range. The formation of a separate glassy silica phase is also supported by the crystallization of cristobalite in samples exposed to high-temperature DSC measurements (Figure S4 right).

### 3.3. $^{93}$Nb NMR

Fig. 4 shows the $^{93}$Nb MAS-NMR spectra of the present samples. Here, we focus on the central-transition region, which for the glassy component comprises a dominant signal near −1180 ppm, flanked by some spinning sidebands. The latter originate from quadrupolar effects upon the central transition lineshape (described by second-order perturbation theory), combined with the fact that the spinning speed does not exceed the inhomogeneous anisotropic linebroadening and the existence of a distribution of quadrupolar coupling constants.

As previously discussed [26], the spectra of all the glassy components can be fitted assuming a singular Czjzek component, however, the spinning sidebands are not well accounted for in the model, indicating a significant contribution of the chemical shift anisotropy (CSA). Attempts to include a $^{93}$Nb chemical shift anisotropy as an additional fitting parameter, under the assumption that the magnetic shielding and electric field gradient tensors are coincident, did not yield a satisfactory result either. Therefore, to account for the spinning sidebands in our quantitative analysis of the spectra, we calculated the difference between the Czjzek lineshape simulated exclusively for the dominant MAS

**Table 2**
$^{29}$Si isotropic chemical shift, $\delta_{\mathrm{iso}}^{\mathrm{CS}}$, full width at half maximum of the Gaussian component, FWHM, area fraction $f$, and average degree of polymerization of the glass component, $<n>$, obtained from the deconvolution model of the spectra shown in Fig. 3.

| Parameter / Sample | $<n>$ | $Si^2$ | $Si^3$ | $Si^4_{Nb}$ | $Si^4$ | $Li_2SiO_3$ | $Li_2Si_2O_5$ A | $Li_2Si_2O_5$ B |
|---|---|---|---|---|---|---|---|---|
| $\delta_{\mathrm{iso}}^{\mathrm{CS}}$ / ppm (± 0.2) | | −80.9 | −87.0 | −96.8 | −108.7 | −73.3 | −91.4 | −92.8 |
| FWHM / ppm (± 0.5) | | 10.9 | 14.1 | 13.3 | 11.5 | 1.0 | 1.5 | 2.7 |
| $f$ /% (±1) | | | | | | | | |
| 0 min | 2.82 | 28 | 62 | 10 | – | – | – | – |
| 45 min | 2.82 | 28 | 62 | 10 | – | – | – | – |
| 70 min | 2.82 | 28 | 62 | 10 | – | – | – | – |
| 2 h | 2.91 | 25 | 59 | 13 | 3 | – | – | – |
| 24 h | 3.68 | – | 22 | 12 | 34 | 2 | 21 | 10 |

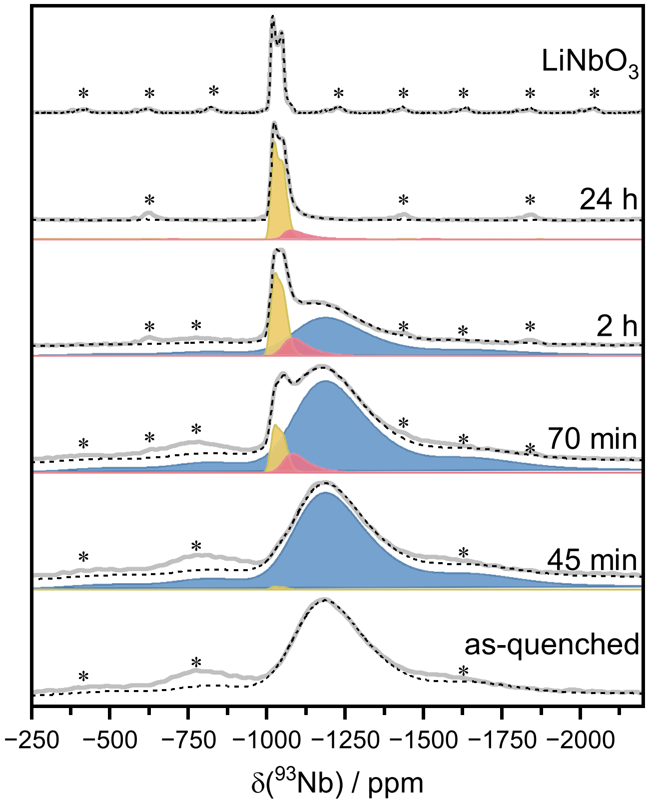

**Fig. 4.** $^{93}$Nb MAS NMR spectra of 35Li$_2$O–25Nb$_2$O$_5$–40SiO$_2$ glass and glass-ceramics under study. Top: $^{93}$Nb MAS NMR spectrum of LiNbO$_3$ at 30.0 kHz MAS rate for comparison. Spinning sidebands are indicated by asterisks. For the LiNbO$_3$ component these arise from the modulation of the eight anisotropically broadened non-central satellite $m_{\mathrm{I}} \leftrightarrow m_{\mathrm{I}}\pm1$ transitions. For the glassy component, the first two sets of spinning sidebands shown within the displayed spectral window are attributed to the central transition region.

central band and the integrated spectrum comprising this dominant MAS central band and the first two sets of magic-angle spinning sidebands. We found that the Czjzek simulation of the dominant MAS central band accounts for 87.7% of the total spectrum attributable to the central $m = ½ \leftrightarrow m = -½$ transition and corrected the area fractions of the glassy component accordingly.

The evolution of the NMR parameters characterizing the $^{93}$Nb MAS-NMR lineshape of the glassy component is summarized in Table 3.

For the glassy component in all samples, the isotropic chemical shift data are within the range of values assigned to six-coordinated niobium [46]. Except for the 24 h sample, the spectra are well fitted by assuming constant $^{93}$Nb interaction parameters of Nb in the residual glassy material at different annealing times. This result, together with the $^{29}$Si MAS NMR data, suggests that the crystallization of LiNbO$_3$ occurs within specific domains that then consist of separate Si$^4$ units, while other domains remain unaltered.

Also, the spectra demonstrate the formation of increasing amounts of LiNbO$_3$ in all the annealed samples, (including a very small amount in the sample annealed for 45 min). Its lineshape is influenced by quadrupolar interactions and can be successfully modeled by second-order perturbation theory. Simulation of the MAS powder pattern using the extended Czjzek model implemented in ssNake yields the parameters summarized in Table 3. The fit can be improved by assuming a narrow distribution of $C_Q$ values, which can be rationalized based on the nanocrystalline character of the lithium niobate compound found in the present samples.

Finally, the spectral simulations reveal a third component featuring the lineshape parameters summarized in Table 3. As this component adopts maximum intensity in samples containing comparable amounts of crystalline and glassy components, we tentatively ascribe this third component to niobium in an interfacial region between nanocrystalline lithium niobate and the residual glassy material, or possibly an amorphous precursor phase to LiNbO$_3$. We obtained further evidence for this component from a $^{93}$Nb MAS NMR spectrum of a glass-ceramic produced in the course of the preliminary investigation of the optimal thermal treatment conditions. This specimen was produced through crystallization treatment at 640 °C for 2 h, identical to the one discussed above, and will be referred to as 2 h-B for clarity. Figure S5.a shows a comparison of the $^{93}$Nb MAS NMR spectra of the glass-ceramic under study produced after 24 h annealing and sample 2 h-B. The green curve represents the difference between both spectra and highlights the lower amount of the interfacial Nb environment in the sample crystallized for 24 h. Figure S5.b additionally shows 3QMAS NMR spectra of the sample 2 h-B in superposition with a spectrum of LiNbO$_3$, further demonstrating additional signal intensity in the spectral region from −1060 to −1100 ppm.

### 3.4. $^{7}$Li dipolar NMR spectroscopy

Fig. 5a shows the results from $^{7}$Li static spin-echo decay spectroscopy. As discussed previously [13,32], this method probes the strength of the homonuclear magnetic dipole-dipole coupling among the $^{7}$Li spins by providing average values of dipolar second moments $M_{2E(\text{Li-Li})}$, which can be compared with predictions from computationally generated models. The results are summarized in Table 4. As previously shown for glasses of the present system [26] and – in a similar study – for quenched and thermally relaxed lithium disilicate glasses [13], the validity of the data in terms of their significance concerning the determination of $M_{2E(\text{Li-Li})}$ is limited to the data range $0 \leq 2\tau_1 \leq 100$ µs.

As indicated by Table 4, the variations in $M_{2E(\text{Li-Li})}$ between the different samples heated between zero and 2 h are within experimental error. For samples at the heating stages 45 min, 70 min, and 120 min this may not seem very surprising as the fraction of crystallized LiNbO$_3$ is rather low. However, this result also allows the conclusion that the annealing leading to the gradual crystallization of LiNbO$_3$ from the glass in those samples has no discernable impact on the spatial distribution of the lithium ions remaining in the residual glassy material.

In the sample heated for 24 h, the situation is more complex, as the

**Table 3**
$^{93}$Nb NMR parameters extracted from the deconvolution model of the experimental spectra shown in Fig. 4. The area fraction of the glass component was corrected by a factor of $f = 0.877$, accounting for the discrepancy between the Czjzek model applied to the dominant MAS center band only and the experimental spectrum of the base glass.

| Parameter / Sample | Glass Component | Interfacial Glass Component | $LiNbO_3$ Component |
|---|---|---|---|
| $\delta_{iso}^{CS}$ / ppm (± 5) | −1092 | −1050 (−1043*) | −1005 |
| $\overline{\lvert C_Q \rvert}$ ($\sigma$) / MHz (± 2) | 4.8 (25.1) | 27.9 (14.0) | 23.4 (1.7) |
| $C_{Q,0}$ ($\eta_0$) / MHz (± 2) | – | – | 23.3 (0.0) |
| FWHM GB / ppm (± 5) | 177 | 22 (30*) | 50 (15*) |
| $f$ /% (±2) | | | |
| 0 min | 100 | – | – |
| 45 min | >99 | – | <1 |
| 70 min | 91 | 5 | 4 |
| 2 h | 74 | 8 | 18 |
| 24 h | 0 | 15 | 85 |

[*] Values apply to the sample annealed for 24 h.

lithium inventory of this sample comprises a considerable amount of (1) lithium in the form of crystalline $Li_2Si_2O_5$ (as indicated by the $^{29}$Si MAS-NMR), (2) lithium in the residual glass, as well as (3) lithium in the crystalline $LiNbO_3$ (as Fig. 4 illustrates 85% of the niobium content has crystallized into $LiNbO_3$). Here the data suggest the presence of a second regime of validity (green line in Fig. 5a), within the data range 160 μs ≤ $2\tau_1$ ≤ 200 μs, in which the experimental $M_{2E(Li\text{-}Li)}$ of 36× $10^6$ rad$^2$s$^{-2}$ closely matches the one of 34.1 × $10^6$ rad$^2$s$^{-2}$ calculated by Eq. (3) from the crystal structure of $LiNbO_3$ [47]. Fig. 5b shows the $^7$Li{$^{93}$Nb} W-RESPDOR dephasing curves of the samples under study. The second moments obtained from a parabolic fit of the data according to Eq. (4) for the as-quenched glass stand in good agreement with a previous measurement [26]. However, in contrast to the results from $^7$Li spin echo decay, significant changes in the heteronuclear dipolar coupling strength can be observed for the glass-ceramics: The $M_{2(Li\text{-}Nb)}$ values increase monotonically as a function of crystallization time, reflecting the shorter effective Li···Nb distance of about 2.24 Å in the formed $LiNbO_3$ compared to the effective two-spin distance in the residual glass of 3.25 Å. As the amount of lithium niobate keeps increasing with increasing annealing time, so does the fraction of lithium that closely interacts with niobium. Finally, the $M_{2(Li\text{-}Nb)}$ value of the 24 h sample matches the value measured for $LiNbO_3$. Both values are somewhat lower compared to the theoretical value of 271.1 × $10^6$ rad$^2$/s$^2$ calculated via Eq. (5) from the crystal structure of this compound[47], however, the uncertainty of the fits is much larger than for the other

**Table 4**
$^7$Li homonuclear $^7$Li–$^7$Li ($M_{2E(Li\text{–}Li)}$), and heteronuclear ($M_{2(Li\text{–}Nb)}$) dipolar second moments, for samples under study.

| Sample | $M_{2E(Li\text{–}Li)}$ / $10^6$ rad$^2$/s$^2$ (± 2.5 × $10^6$ rad$^2$/s$^2$) | $M_{2(Li\text{–}Nb)}$ / $10^6$ rad$^2$/s$^2$ (± 5 × $10^6$ rad$^2$/s$^2$) |
|---|---|---|
| 0 min | 88.8 | 29 |
| 45 min | 92.5 | 33 |
| 70 min | 89.8 | 37 |
| 2 h | 91.5 | 40 |
| 24 h | 84.7 / 36.3[a] | 181 (± 20) |
| $LiNbO_3$ | – | 171 (± 20) |

[a] Attributed to $LiNbO_3$

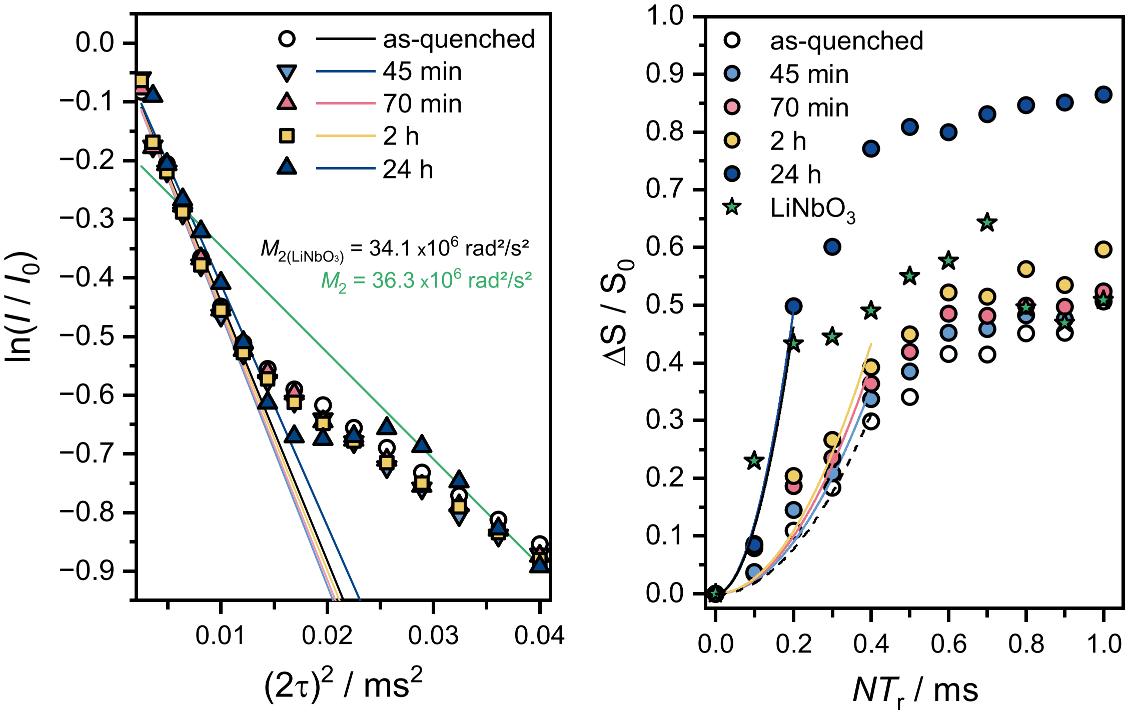

**Fig. 5.** $^7$Li spin echo decay (a) and $^7$Li{$^{93}$Nb}W-RESPDOR dephasing (b) curves of $35Li_2O$–$25Nb_2O_5$–$40SiO_2$ glass and glass-ceramics under study. Solid curves denote fits to Eqs. (2) and (4), respectively.

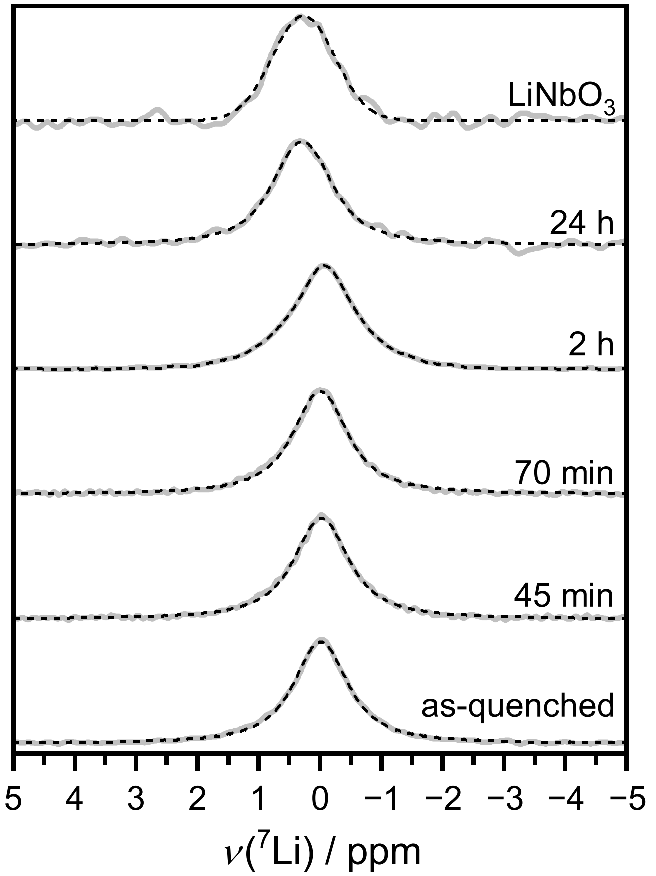

**Fig. 6.** $^6$Li MAS NMR spectra of specimens under study. The gray and dashed black lines are the experimental data and fit, respectively.

samples. In addition, the RESPDOR curve of this sample always contains a contribution from lithium ions in the crystalline lattice of $Li_2Si_2O_5$ that do not contribute to the signal dephasing

Overall, the complementary results from the above dipolar spectroscopies give further evidence that the crystallization of $LiNbO_3$ occurs in specific domains leaving the $Li^+$ ion distribution in the residual glass largely unchanged.

### 3.5. $^6$Li MAS-NMR

In principle, any changes in the lithium local environment due to crystallization are expected to affect the magnetic shielding (chemical shifts) experienced by the $^7$Li nuclei. In practice, however, $^7$Li chemical shifts are fairly insensitive to changes in Li coordination environments, bond lengths and angles, and vary within a few ppm only, and the $^7$Li MAS-NMR linewidths are affected by both residual $^7$Li-$^7$Li dipole-dipole couplings and $^7$Li quadrupolar couplings, not completely averaged by MAS. In principle, the NMR spectra of the less abundant isotope $^6$Li ($I = 1$) should be better resolved than those of their $^7$Li counterparts due to the 60 times smaller quadrupole moment and the smaller magnetic dipole moment of the $^6$Li nucleus. Thus, chemical shift differences between different local environments should be resolvable more easily by $^6$Li MAS-NMR than by $^7$Li MAS-NMR. Indeed, it was shown that $^6$Li chemical shifts correlate well with the coordination number of the lithium species [48]. Fig. 6 shows the $^6$Li MAS-NMR spectra of $LiNbO_3$ nanoparticles and the samples under study.

**Table 5**
$^6$Li NMR lineshape parameters and $^7$Li Czjzek distribution parameters, the total frequency spans of the SATRAS spectra (Δ), and the area fraction of the integrated difference spectra compared to the entire SATRAS spectrum, *f*, of the samples under study.

| Sample | ($^6$Li) $\delta_{iso}^{CS}$ / ppm | ($^6$Li) FWHM / Hz | Gauss/ Lorentz ratio | ($^7$Li) $\overline{\lvert C_Q \rvert}$ ($\sigma$) / kHz (± 2) | ($^7$Li) Δ / kHz (± 5) | ($^7$Li) *f* / % (±1) |
|---|---|---|---|---|---|---|
| 0 min | −0.01 | 90 | 0.44 | 127 (64) | 240 | – |
| 45 min | −0.02 | 91 | 0.46 | 122 (61) | 240 | 4.4 |
| 70 min | −0.04 | 92 | 0.47 | 119 (59) | 220 | 7.9 |
| 2 h | −0.06 | 106 | 0.73 | 118 (58) | 200 | 12.0 |
| 24 h | 0.29 | 99 | 0.76 | 69 (34) | 160 | 76.5 |
| $LiNbO_3$ | 0.27 | 110 | 0.89 | – | – | – |

The spectra can be satisfactorily modeled with Gauss-Lorentzian lineshapes, whose parameters are summarized in Table 5.

The spectrum of the $LiNbO_3$ nanoparticles is centered at 0.27 ppm, which stands in good agreement with the previously reported chemical shift of 0.33 ppm for bulk $LiNbO_3$ but shows a significantly higher linewidth of 110 Hz (compared to 37.9 Hz for bulk $LiNbO_3$) [49]. The as-quenched glass exhibits a slightly narrower line with a width of 90 Hz centered at 0 ppm. Only subtle lineshape changes can be observed for the spectra of the glass-ceramics up to a crystallization time of 2 h. For the 24 h sample, the center of the line shifts from 0 to 0.29 ppm and increases in width to 99 Hz, consistent with the formation of $LiNbO_3$. The lithium inventory of this sample comprises contributions from three different components ($LiNbO_3$, $Li_2Si_2O_5$, and residual glass). Evidently, the chemical shifts of these components are too close for their contributions to be resolvable by $^6$Li MAS-NMR in the present study.

### 3.6. $^7$Li MAS-NMR

Fig. 7 shows results from $^7$Li MAS and satellite transition difference MAS-NMR spectroscopies.

While the MAS central transitions are again handicapped by the limited chemical shift resolution, the MAS-NMR spectra of the $^7$Li nuclei ($I = 3/2$) show additional features arising from the interaction of the $^7$Li nuclear electric quadrupolar moment with local electric field gradients. The latter manifest themselves quite distinctively in the spread and shape of the non-central $|m| = ½ \leftrightarrow |m| = {}^3/_2$ Zeeman transitions ($\Delta m = \pm 1$), also called “satellite” transitions. These are commonly observed and quantified from MAS NMR experiments, in which they produce spinning sideband manifolds. In the slow-spinning limit ($\nu_r \ll \nu_Q$) the spinning sideband intensity pattern forms the envelope of the static powder pattern of the satellite transitions, making it possible to determine the average quadrupolar coupling constants $C_Q$ and electric field gradient asymmetry parameters $\eta_Q$ by simulation (“Satellite transition spectroscopy”, SATRAS). Fig. 7 (left) shows the $^7$Li SATRAS data for the present samples. A total span of 200 ± 2 kHz is observed for the samples up to a heat treatment time of 2 h, while the span of the 24 h glass-ceramic is about 140 ± 2 kHz. While for a glass a distribution of local EFGs around the $^7$Li spins is expected, the total span of the spinning sideband pattern corresponds to the largest EFGs detectable in the glass within the limitations of the signal-to-noise (S/N) ratios. In fact, the spinning sideband profile can be sufficiently well simulated assuming a Czjzek distribution of quadrupolar parameters (data not shown). Notably, however, the distribution widths are rather invariant for the samples under study.

Table 5 summarizes the Czjzek distribution width used to simulate the sideband patterns and the fractional contributions from the crystalline phases and glassy material extracted from SATRAS difference spectroscopy.

As discussed previously [26], interesting changes can be revealed by looking at the SATRAS difference spectra. In our previous contribution, the spectra of a number of heat-treated samples were normalized such that the outermost spinning sidebands exhibit the same intensity as those of the as-quenched sample and, subsequently, the spectrum of the as-quenched sample was subtracted. The residual spectrum is then made up of $^7$Li resonances of the crystalline phases that are not present in the

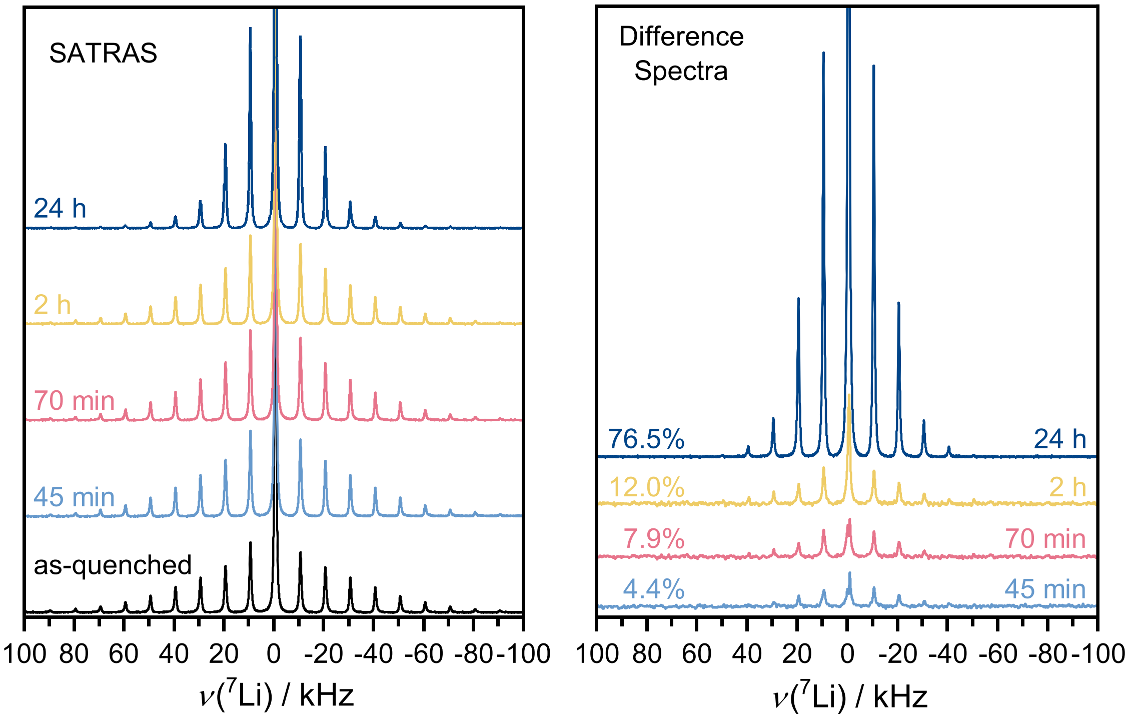

**Fig. 7.** Left: $^7$Li SATRAS NMR spectra of specimens under study. Right: SATRAS difference spectra showing only signal from $^7$Li in crystalline environments. The values shown in the figure are the fractions of the integrated difference spectra compared to the entire SATRAS spectrum.

**Table 6**
Calculation of the total degree of crystallization of $Nb_2O_5$, $SiO_2$, and $Li_2O$, breakdown of the crystalline fraction of $Li_2O$ into crystalline phases based on $^{93}$Nb and $^{29}$Si spectroscopy, and composition of the residual glass.

| Crystalline fraction / % | 45 min | 70 min | 2 h | 24 h |
|---|---|---|---|---|
| **Nb inventory from $^{93}$Nb NMR** | <1 | 4 | 18 | 85 |
| $LiNbO_3$ | | 4 | 18 | 85 |
| **Si inventory from $^{29}$Si NMR** | 0 | 0 | 0 | 33 |
| $Li_2Si_2O_5$ A | – | – | – | 21 |
| $Li_2Si_2O_5$ B | – | – | – | 10 |
| $Li_2SiO_3$ | – | – | – | 2 |
| **Li inventory from $^7$Li NMR** | 4.4 | 7.9 | 12.0 | 76.5 |
| $LiNbO_3$ | 4.4 | 7.9 | 12.0 | 61[a] |
| $Li_2Si_2O_5$ | – | – | – | 18[b] |
| $Li_2SiO_3$ | – | – | – | 2[b] |
| **Total ($Nb_2O_5$ + $SiO_2$ + $Li_2O$)** | **1.5** | **4.0** | **10.0** | **61.2** |
| Residual Glass Composition / mol% | | | | |
| $Li_2O$ | 0.35 | 0.33 | 0.33 | 0.18 |
| $Nb_2O_5$ | 0.25 | 0.25 | 0.22 | 0.10 |
| $SiO_2$ | 0.40 | 0.42 | 0.44 | 0.72 |

[a] from $^{93}$Nb MAS NMR.
[b] from $^{29}$Si MAS NMR.

base glass. This approach worked well for a stoichiometric LS2 glass in which the composition of the residual glass stays rather invariant upon crystallization [13]. For nonstoichiometric glasses on the other hand, changes in the residual glass during heat treatment may produce changes in the $^7$Li EFG distribution which do not stem from the crystalline fraction exclusively. A better approach in such a case is constructing SATRAS difference spectra from two measurements of the same glass-ceramic sample using different recycle delays, exploiting the differences in longitudinal relaxation times $T_1$ of the vitreous and crystalline parts.

Figure S6 shows the $^7$Li saturation recovery curve of glass-ceramic annealed at 24 h which was fitted to a mono exponential function, yielding a $T_1$ value of 13.5 s. Under these circumstances, performing a measurement using a recycle delay of 160 s yields a quantitative spectrum (magnetization $I = 99.998\%$) while the same experiment with a recycle delay of 0.1 s should contain nearly no intensity from $^7$Li in crystalline environments ($I = 0.663\%$). Figure S7 shows that recycle delays of 0.1 and 1 s already yield identical SATRAS profiles at the given S/N ratio using the example of the 2 h sample. At this point, it is further worth pointing out that in Nb-free, stoichiometric LS2 glass-ceramics, the $^7$Li relaxation times of the crystalline components are much longer ($T_1 \sim 80$ s) than found in the present system. The much shorter relaxation time in the samples under study – measurements with a recycle delay of 900 s showed no difference to measurements using 160 s – is consistent with significant interaction between the $^7$Li spins in the LS2 phase and fluctuating $^{93}$Nb spins in some proximity near the interface (the fluctuations may arise from electric field gradient modulations by low-frequency vibrational modes). Alternatively, the short $T_1$ values could arise from the nanocrystalline character of LS2 and/or a high specific surface area or from the presence of paramagnetic impurities.

The difference spectra of all glass-ceramics are shown in Fig. 7 (right). The spectra are much narrower than the $^7$Li SATRAS spectra and show that both, the crystalline $LiNbO_3$ and $Li_2Si_2O_5$ present in samples annealed for 2 and 24 h make significant lineshape contributions not present in the base glass:

In the glass-ceramic samples produced at annealing times beyond 45 min, the spinning sideband profiles of the SATRAS difference spectra become slightly broader. For the samples heat-treated for 2 h and 24 h, the area fractions of the $^7$Li SATRAS difference spectra (compared to the regular SATRAS spectrum of each sample) are 12.0 and 76.5%, respectively. We attribute this SATRAS difference intensity to the crystalline fractions of $LiNbO_3$ and $Li_2Si_2O_5$ and point out the much higher precision of this quantification approach compared to $^{29}$Si or $^{93}$Nb MAS NMR. Clearly, in the present case, the $^7$Li SATRAS difference spectra prove to be much more sensitive to changes in the local environment of the nuclei than the $^6$Li MAS NMR spectra. However, the quantitative SATRAS results of Fig. 7 are fully consistent with the qualitative trend suggested by the average $^6$Li chemical shift changes documented in Table 4.

### 3.7. Calculation of crystallinity and residual glass composition

Based on the complementary quantitative information gathered above, which are summarized in Table 6, we can consistently formulate the following quantitative model for the crystallization of glass with composition $35Li_2O–25Nb_2O_5–40SiO_2$:

$$35Li_2O-25Nb_2O_5-40SiO_2 \rightarrow 42.5LiNbO_3+6.2Li_2Si_2O_5+0.8Li_2SiO_3 + \text{ glass } (6.8Li_2O-3.7Nb_2O_5-26.8SiO_2)$$

Thus, the lithium-to-silicon ratio of the residual lithium silicate glass (neglecting the small amount of residual niobium oxide not present as crystalline $LiNbO_3$) corresponds to the composition of a binary lithium silicate glass having 20.2 mol% $Li_2O$. Thus, the residual glass is – at least on average – much more dilute in lithium than the glassy precursor. In addition, in view of the $^{29}Si$ spectrum of Fig. 3 the residual glass cannot be considered a homogeneous phase. Rather we conclude that the crystallization process occurs within fixed domains from which the Li content is extracted to promote the formation of $LiNbO_3$, leaving behind an amorphous silica component.

Note that considering only the average Li/Si ratio of the remaining glassy phase would imply an average degree of polymerization $<n>$ of 3.50, whereas the $^{29}Si$ MAS NMR spectrum (Table 2) indicates a degree of polymerization of 3.67. However, it was previously shown that niobium acts as network former in silicate glasses [26], forming negatively charged $NbO^{-}_{6/2}$ octahedra. Considering the previous result that one mole of $Nb_2O_5$ requires on average about 0.7 equivalents in $Li_2O$ for charge compensation in this glass composition [26], taking this modifier demand into consideration, the degree of polymerization of the silicate network is recalculated as 3.69, which is more consistent with the experimental data. According to satellite difference spectroscopy, 76.5% of the $Li_2O$ inventory is crystallized after annealing for 24 h. Based on $^{93}Nb$ and $^{29}Si$ MAS NMR, the amount of formed $LiNbO_3$, $Li_2Si_2O_5$, and $Li_2SiO_3$ require a total of 80.7% of the $Li_2O$ inventory, which stands in excellent agreement with the $^7Li$ NMR data.

## 4. Conclusions

Our study shows how multinuclear NMR is sensitive to the crystalline phases and vitreous material in the studied $LiNbO_3–SiO_2$ glass-ceramics and provides a quantification that is consistent across all of the employed spectroscopies. Among the herein used techniques, $^7Li$ SATRAS difference NMR spectroscopy stands out with its high sensitivity for changes in the local environment of the network modifier, which allows the detection and quantification of much lower concentrations of crystalline phases than possible by X-ray scattering or Raman spectroscopy. While this technique is not readily able to distinguish between the changes the $^7Li$ ions experience under heat treatment of the glass, it serves as a fast and straightforward method to determine the total degree of crystallinity of glass-ceramics, even in the case of non-stoichiometric crystallization, as in the present case.

Crystallization of the present system proceeds within Nb-containing glassy domains, from which the Nb and Li species are extracted to form lithium niobate, leaving behind unmodified vitreous $SiO_2$ ($Q^4$ species). At long annealing times, crystalline lithium disilicate and some metasilicate are formed as well. From the quantitative analysis of the silicon, niobium, and lithium inventories via the corresponding advanced MAS-NMR approaches it was possible to derive the quantitative phase distribution and the chemical composition of the residual glassy material at different annealing stages. The solid-state NMR strategy developed in the present study represents the first use of this technique for a detailed quantitative characterization of glass-ceramics crystallizing in a non-stoichiometric glass system, where the composition of the main crystallized phase does not correspond to the glass composition. To the best of our knowledge, it also represents the first quantitative application to a niobium-based glass-ceramic system. We expect that it will be applicable or adaptable to similar and other complex structural issues in a variety of glasses, glass-ceramics, and nanocomposites.

## CRediT authorship contribution statement

**Henrik Bradtmüller:** Writing – original draft, Visualization, Methodology, Investigation, Funding acquisition, Formal analysis, Conceptualization. **Qiuju Zheng:** Writing – review & editing, Resources, Investigation, Conceptualization. **Hellmut Eckert:** Writing – original draft, Resources, Funding acquisition, Formal analysis, Conceptualization. **Edgar D. Zanotto:** Writing – review & editing, Supervision, Resources, Project administration, Funding acquisition, Conceptualization.

## Declaration of competing interest

The authors declare that they have no known competing financial interests or personal relationships that could have appeared to influence the work reported in this paper.

## Data availability

Data will be made available on request.

## Acknowledgments

This work was supported by the São Paulo Research Foundation (FAPESP) under grant no. 2013/07793–6 (CEPID program). H.B. is grateful for the post-doctoral support received from FAPESP under grant number 2019/26399–3. HE (310870/2020–8) and EDZ (303886/2015–3) are grateful to CNPq for a Bolsa de Pesquisa Grant. Finally, QZ and EDZ are grateful to CBMM (Cia. Brasileira de Mineração e Metalurgia) for research grants dedicated to revealing the role of $Nb_2O_5$ in the physical-chemical properties of silicate glasses.

## Supplementary materials

Supplementary material associated with this article can be found, in the online version, at doi:10.1016/j.jnoncrysol.2024.123096.

## References

[1] X. Liu, J. Qiu, 7 - Nonlinear photonics in glasses, in: G.C. Righini, L. Sirleto (Eds.), Advances in Nonlinear Photonics, Woodhead Publishing, 2023, pp. 177–213.
[2] O.G. Morales–Saavedra, E. Chavira, Synthesis–dependent structural and optoelectronic properties of semicrystalline $LiNbO_3$:$SiO_2$ hybrid silicates, Opt. Mater. 142 (2023) 113930.
[3] J. Deubener, M. Allix, M.J. Davis, A. Duran, T. Höche, T. Honma, T. Komatsu, S. Krüger, I. Mitra, R. Müller, S. Nakane, M.J. Pascual, J.W.P. Schmelzer, E. D. Zanotto, S. Zhou, Updated definition of glass-ceramics, J. Non Cryst. Solids 501 (2018) 3–10.
[4] X. Feng, J. Qiu, S. Zhou, Synergistic effect in nonlinear response in glass ceramics, J. Am. Ceram. Soc. 107 (3) (2024) 1936–1948.
[5] X. Feng, Y. Lun, X. Jiang, J. Qiu, H. Yu, S. Zhou, Manipulating nonlinear optical response via domain control in nanocrystal-in-glass composites, Adv. Mater. 33 (2021) 2006482.
[6] K.S. Gerace, M.T. Lanagan, J.C. Mauro, Dielectric polarizability of $SiO_2$ in niobiosilicate glasses, J. Am. Ceram. Soc. 106 (2023) 4546–4553.
[7] A. Chakrabarti, S. Chatterjee, A.R. Molla, A. Ghosh, Sodium niobate-based glass-ceramics: Dependence of crystallization temperature on phase evolution, refractive index and dielectric properties, J. Non Cryst. Solids. 625 (2024) 122773.
[8] J. Lubauer, R. Belli, A. Petschelt, M.R. Cicconi, K. Hurle, U. Lohbauer, Concurrent kinetics of crystallization and toughening in multicomponent biomedical $SiO_2$-$Li_2O$-$P_2O_5$-$ZrO_2$ glass-ceramics, J. Non Cryst. Solids 554 (2021) 120607.
[9] K. Hurle, R. Belli, F. Götz-Neunhoeffer, U. Lohbauer, Phase characterization of lithium silicate biomedical glass-ceramics produced by two-stage crystallization, J. Non Cryst. Solids 510 (2019) 42–50.
[10] C. Schröder, J. Ren, A.C.M. Rodrigues, H. Eckert, Glass-to-crystal transition in $Li_{1+x}Al_xGe_{2-x}(PO_4)_3$: Structural aspects studied by solid state NMR, J. Phys. Chem. C 118 (2014) 9400–9411.
[11] C. Bischoff, H. Eckert, E. Apel, V.M. Rheinberger, W. Höland, Phase evolution in lithium disilicate glass–ceramics based on non-stoichiometric compositions of a

multi-component system: structural studies by $^{29}$Si single and double resonance solid state NMR, Phys. Chem. Chem. Phys. 13 (2011) 4540–4551.

[12] P. Soares Jr, E. Zanotto, V. Fokin, H. Jain, TEM and XRD study of early crystallization of lithium disilicate glasses, J. Non Cryst. Solids 331 (2003) 217–227.

[13] H. Bradtmüller, A. Gaddam, H. Eckert, E.D. Zanotto, Structural rearrangements during sub-$T_g$ relaxation and nucleation in lithium disilicate glass revealed by a solid-state NMR and MD strategy, Acta Mater. (2022) 118318.

[14] W.C. Liao, M. Rampf, M. Dittmer, C. Copéret, W. Höland, Nucleation and crystal formation in lithium disilicate-apatite glass-ceramic from a combined use of x-ray diffraction, solid-state NMR, and microscopy, Helv. Chim. Acta 102 (2019).

[15] A. Ananthanarayanan, G. Tricot, G.P. Kothiyal, L. Montagne, A comparative overview of glass-ceramic characterization by MAS-NMR and XRD, Crit. Rev. Solid State Mater. Sci. 36 (2011) 229–241.

[16] M. Montazerian, M. Mancini, J.C. Mauro, Advanced tools for unveiling nucleation in nanostructured glass-ceramics, Crit. Rev. Solid State Mater. Sci. 48 (2023) 411–439.

[17] Z. Liu, S. Venkatachalam, H. Kirchhain, L. van Wüllen, Study of the glass-to-crystal transformation of the NASICON-type solid electrolyte $Li_{1+x}Al_xGe_{2-x}(PO_4)_3$, Solid. State Ion. 295 (2016) 32–40.

[18] C. Lin, C. Rüssel, L. van Wüllen, Phase Separation and Nanocrystallization in $KF–ZnF_2–SiO_2$ Glasses: Lessons from Solid-State NMR, J. Phys. Chem. B 123 (2019) 1688–1695.

[19] A. Flambard, L. Montagne, L. Delevoye, G. Palavit, J.P. Amoureux, J.J. Videau, Solid-state NMR study of mixed network sodium–niobium phosphate glasses, J. Non Cryst. Solids 345-346 (2004) 75–79.

[20] K.O. Drake, D. Carta, L.J. Skipper, F.E. Sowrey, R.J. Newport, M.E. Smith, A multinuclear solid state NMR study of the sol–gel formation of amorphous $Nb_2O_5–SiO_2$ materials, Solid State Nucl. Magn. Reson. 27 (2005) 28–36.

[21] S. Chenu, U. Werner-Zwanziger, C. Calahoo, J.W. Zwanziger, Structure and properties of $NaPO_3–ZnO–Nb_2O_5–Al_2O_3$ glasses, J. Non-Cryst. Solids 358 (2012) 1795–1805.

[22] P. Kalenda, L. Koudelka, P. Mošner, L. Montagne, B. Revel, J. Trebosc, Glass to crystal transformation in the ternary $BaO-Nb_2O_5-P_2O_5$ system, J. Mol. Struct. 1143 (2017) 472–477.

[23] M. Dolhen, M. Allix, V. Sarou-Kanian, F. Fayon, C. Genevois, S. Chenu, P.E. Coulon, M. Colas, J. Cornette, J.R. Duclère, F. Brisset, O. Masson, P. Thomas, G. Delaizir, A comprehensive study of the glass/translucent anti-glass/transparent ceramic structural ordering in the $Bi_2O_3-Nb_2O_5-TeO_2$ system, Acta Mater. 189 (2020) 73–84.

[24] L.M. Marcondes, H. Bradtmüller, S.N. Carvalho dos Santos, L.K. Nolasco, C. R. Mendonça, S.H. Santagneli, G.Y. Poirier, M. Nalin, Structural and luminescence characterization of europium-doped niobium germanate glasses and glass-ceramics: Novel insights from $^{93}$Nb solid-state NMR spectroscopy, Ceram. Int. 48 (2022) 20801–20808.

[25] J.H. Faleiro, N.O. Dantas, A.C.A. Silva, H.P. Barbosa, B.H.S.T. da Silva, K.d. O. Lima, G.d.F. Silva, R.R. Gonçalves, R. Falci, Y. Messadeq, I.D.d.O. Branco, B. M. Cerrutti, H. Bradtmüller, H. Eckert, J.L. Ferrari, Niobium incorporation into rare-earth doped aluminophosphate glasses: Structural characterization, optical properties, and luminescence, J. Non Cryst. Solids 605 (2023) 122173.

[26] H. Bradtmüller, Q. Zheng, A. Gaddam, H. Eckert, E.D. Zanotto, Structural impact of niobium oxide on lithium silicate glasses: Results from advanced interaction-selective solid-state nuclear magnetic resonance and Raman spectroscopy, Acta Mater. 255 (2023) 119061.

[27] M.J.F. Costa, A.A.S. Gonçalves, R. Rinaldi, H. Bradtmüller, H. Eckert, E.B. Ferreira, Highly porous niobium-containing silica glasses applied to the microwave-assisted conversion of fructose into HMF, Catal. Commun. 174 (2023) 106577.

[28] H. Vigouroux, E. Fargin, S. Gomez, B. Le Garrec, G. Mountrichas, E. Kamitsos, F. Adamietz, M. Dussauze, V. Rodriguez, Synthesis and Multiscale Evaluation of $LiNbO_3$-Containing Silicate Glass-Ceramics with Efficient Isotropic SHG Response, Adv. Funct. Mater. 22 (19) (2012) 3985–3993.

[29] S.G.J. van Meerten, W.M.J. Franssen, A.P.M. Kentgens, ssNake: A cross-platform open-source NMR data processing and fitting application, J. Magn. Reson. 301 (2019) 56–66.

[30] G.L. Caër, R.A. Brand, General models for the distributions of electric field gradients in disordered solids, J. Phys.: Condens. Matter 10 (1998) 10715.

[31] C. Jäger, W. Müller-Warmuth, C. Mundus, L. van Wüllen, $^{27}$Al MAS-NMR spectroscopy of glasses: new facilities by application of ‘SATRAS, J. Non Cryst. Solids 149 (1992) 209–217.

[32] J.G. Longstaffe, U. Werner-Zwanziger, J.F. Schneider, M.L. Nascimento, E. D. Zanotto, J.W. Zwanziger, Intermediate-range order of alkali disilicate glasses and its relation to the devitrification mechanism, J. Phys. Chem. C 112 (2008) 6151–6159.

[33] D. Lathrop, D. Franke, R. Maxwell, T. Tepe, R. Flesher, Z. Zhang, H. Eckert, Dipolar $^{31}$P NMR spectroscopy of crystalline inorganic phosphorus compounds, Solid State Nucl, Magn. Reson. 1 (1992) 73–83.

[34] B. Gee, H. Eckert, $^{23}$Na nuclear magnetic resonance spin echo decay spectroscopy of sodium silicate glasses and crystalline model compounds, Solid State Nucl. Magn. Reson. 5 (1995) 113–122.

[35] J.H. Van Vleck, The dipolar broadening of magnetic resonance lines in crystals, Phys. Rev. 74 (1948) 1168.

[36] J. Haase, E. Oldfield, Spin-echo behavior of nonintegral-spin quadrupolar nuclei in inorganic solids, J. Magn. Reson. A 101 (1993) 30–40.

[37] M. Makrinich, E. Nimerovsky, A. Goldbourt, Pushing the limit of NMR-based distance measurements – retrieving dipolar couplings to spins with extensively large quadrupolar frequencies, Solid State Nucl. Magn. Reson. 92 (2018) 19–24.

[38] E. Kupce, R. Freeman, Adiabatic pulses for wideband inversion and broadband decoupling, J. Magn. Reson. A 115 (1995) 273–276.

[39] A.L. Wübker, J. Koppe, H. Bradtmüller, L. Keweloh, D. Pleschka, W. Uhl, M. R. Hansen, H. Eckert, Solid-state nuclear magnetic resonance techniques for the structural characterization of geminal alane-phosphane frustrated lewis pairs and secondary adducts, Chem. Eur. J. 27 (2021) 13249–13257.

[40] M. Bak, J.T. Rasmussen, N.C. Nielsen, SIMPSON: A general simulation program for solid-state NMR spectroscopy, J. Magn. Reson. 147 (2000) 296–330.

[41] R.J. Cava, A. Santoro, D.W. Murphy, S. Zahurak, R.S. Roth, The structures of lithium-inserted metal oxides: $LiReO_3$ and $Li_2ReO_3$, J. Solid State Chem. 42 (3) (1982) 251–262.

[42] H. Vigouroux, E. Fargin, B.L. Garrec, M. Dussauze, V. Rodriguez, F. Adamietz, J. Ravaux, R. Podor, S. Lotarev, V. Sigaev, In situ study of the crystallization mechanism in $LiNbO_3–SiO_2$ glasses, Physics and Chemistry of Glasses-European Journal of Glass Science and Technology Part B 54 (2013) 84–88.

[43] M.R. Cicconi, D.K. Dobesh, B. Schroeder, T. Otsuka, T. Hayakawa, D. de Ligny, Alkali-Niobate aluminosilicate glasses: Structure and properties, Opt. Mater. X 18 (2023) 100228.

[44] X. Yang, G. Lan, B. Li, H. Wang, Raman spectra and directional dispersion in $LiNbO_3$ and $LiTaO_3$, Phys. Status Solidi (b) 142 (1987) 287–300.

[45] V.S. Gorelik, S.D. Abdurakhmonov, N.V. Sidorov, M.N. Palatnikov, Raman scattering in lithium niobate and Llithium tantalate single crystals and ceramics, Inorg. Mater. 55 (2019) 524–532.

[46] O.B. Lapina, D.F. Khabibulin, K.V. Romanenko, Z. Gan, M.G. Zuev, V. N. Krasil`nikov, V.E. Fedorov, $^{93}$Nb NMR chemical shift scale for niobia systems, Solid State Nucl. Magn. Reson. 28 (2005) 204–224.

[47] R. Hsu, E.N. Maslen, D. du Boulay, N. Ishizawa, Synchrotron X-ray Studies of $LiNbO_3$ and $LiTaO_3$, Acta Crystallogr. B 53 (3) (1997) 420–428.

[48] Z. Xu, J.F. Stebbins, $^6$Li nuclear magnetic resonance chemical shifts, coordination number and relaxation in crystalline and glassy silicates, Solid. State Nucl. Magn. Reson. 5 (1995) 103–112.

[49] Y. Xia, N. Machida, X. Wu, C. Lakeman, L. van Wüllen, F. Lange, C. Levi, H. Eckert, S. Anderson, $^7$Li and $^6$Li Solid-State NMR Studies of Structure and Dynamics in $LiNbO_3-WO_3$ Solid Solutions, J. Phys. Chem. B 101 (1997) 9180–9187.